Near-bandgap harmonic generation in solids from multiple scattering revealed by complex quantum trajectories

Xunqin Huo,[1,2] Xiwang Liu,[1] Shidong Yang,[1,2] Xiaohong Song,[1,*] Torsten Meier,[3] and Weifeng Yang[1,4,†]

[1]*School of Physics and Optoelectronic Engineering, Hainan University, Haikou 570228, China*

[2]*School of Information and Communication Engineering, Hainan University, Haikou 570228, China*

[3]*Department of Physics and Institute for Photonic Quantum Systems (PhoQS), Paderborn University, Warburger Straße 100, D-33098 Paderborn, Germany*

[4]*Center for Theoretical Physics, Hainan University, Haikou 570228, China*

(Received 17 May 2026; accepted 27 August 2026; published 11 September 2026)

High-harmonic generation in solids enables probing of strong-field electron dynamics in condensed matter and the development of compact ultrafast light sources. Whereas most studies have focused on above-bandgap high-order harmonics, which are usually interpreted through short electron-hole trajectories that recombine within one optical cycle, the microscopic origin of low-order emission near the bandgap remains poorly understood. Here, we investigate near-bandgap harmonic generation in ZnO by combining semiconductor Bloch equations with a complex-time quantum-trajectory analysis. Our results indicate that these harmonics are not a continuation of the short trajectory. Rather, they originate from multiple-scattering trajectories, in which the electron-hole pair undergoes repeated Bragg scattering at the Brillouin-zone boundary and electron-hole reencounter near the Γ point before the actual recombination occurs. We identify that the imaginary part of the electron-hole displacement provides a practical diagnostic of the residual tunneling memory. Real-space electron-hole overlap alone does not imply coherent recombination unless the full complex displacement vanishes. These results clarify the microscopic picture of near-bandgap harmonic emission in ZnO and offer a framework for interpreting phase-resolved strong-field dynamics in solids.

DOI: 10.1103/l939-jglf

I. INTRODUCTION

High-harmonic generation (HHG) is a central nonlinear process in strong-field physics, producing coherent extreme-ultraviolet radiation and attosecond pulses [1–4]. In gases, HHG is well described by the three-step model [5]. Extending HHG to crystalline solids has opened a rich research frontier, where the periodic lattice potential and electronic band structure introduce qualitatively new dynamical channels. Solid-state HHG has become a powerful probe of ultrafast carrier dynamics in condensed matter and a promising route toward compact attosecond light sources [6–13]. Most previous work has focused on above-bandgap higher-order harmonics [14–17]. The microscopic origin of low-order harmonics near the bandgap, however, remains much less clear, despite their prominence in semiconductors and dielectrics.

In atomic and molecular systems, near-threshold and below-threshold harmonics are known to originate from mechanisms beyond the standard three-step picture [5], including multiple rescattering [18–25], excited-state channels [19], and Rydberg-mediated pathways [26–28]. These studies indicate that near-threshold harmonic emission can encode dynamics that are qualitatively different from those responsible for above-threshold harmonics.

In solids, HHG is commonly described in terms of interband polarization associated with electron-hole recombination and intraband motion driven by Bloch oscillations [14–17,29]. Strong-field-induced injection currents associated with subcycle population transfer across the bandgap constitute an additional source of low-order, below-bandgap harmonics [30]. This contribution is generated during the tunneling-induced carrier-injection step itself and is therefore distinct from the interband-recombination process considered here. The solid-state extension of the semiclassical three-step model has provided a useful framework for interpreting many features of HHG in crystals. However, conventional semiclassical treatments often neglect the dynamics of the tunneling [14,15,31], an approximation that becomes problematic for phase-sensitive observables such as two-color interferometry [32–38]. Complex quantum-trajectory approaches that explicitly retain tunneling dynamics have substantially improved the description of solid-state HHG, yet noticeable discrepancies remain in the near-bandgap region [38,39].

A key insight from the theory of atomic HHG is that strong-field tunneling naturally leads to complex saddle-point variables [40]. In the solid-state extension, the ionization time, canonical momentum, and relative electron-hole displacement

*Contact author: song_xiaohong@hainanu.edu.cn

†Contact author: wfyang@hainanu.edu.cn

generally become complex valued. The imaginary part of the displacement carries the memory of underbarrier motion and imposes an additional constraint on coherent recombination. Crucially, in HHG, it is the photon energy that must be real, not the electron momentum [40]. Consequently, the imaginary part of the canonical momentum can be substantial, and the active electron is not a free photoelectron but retains an evanescent character from the tunneling step. These insights provide the conceptual basis for applying complex quantum trajectories to solid-state HHG. Here, the bandgap assumes the role of the ionization potential. The central question addressed here is how this complex displacement should be interpreted in a periodic crystal, where, unlike in atoms, the electron-hole motion is governed by Bloch-band dynamics and Bragg scattering rather than by Coulomb-driven recollision.

In this paper, we combine semiconductor Bloch equations (SBEs) with a complex-time saddle-point analysis to identify the trajectory origin of near-bandgap harmonic generation in ZnO. We show that the short trajectory, where tunneling and recombination occur within the same optical cycle, accurately describes higher-order harmonics but fails in the near-bandgap region. The missing contribution is associated with a delayed multiple-scattering trajectory, in which the electron-hole pair is born one optical cycle earlier and is repeatedly redirected by the periodic band structure through Bragg scattering at the Brillouin-zone (BZ) boundary and field-driven electron-hole reencounter near the Γ point before recombination. We further show that the imaginary part of the relative electron-hole displacement provides a practical criterion for distinguishing coherent recombination from scattering-induced real-space overlap. This analysis yields a unified microscopic picture of near-bandgap HHG in solids.

II. THEORETICAL METHODS

A. Semiconductor Bloch equations

We analyze HHG in solids within an SBE framework, the standard theoretical description of laser-driven electron-hole dynamics and interband transitions in crystals [14,15,41,42]. The SBEs read

$$\dot{\pi}(\mathbf{K},t) = -\frac{1}{T_2}\pi(\mathbf{K},t) - i\Omega(\mathbf{K},t)\,w(\mathbf{K},t)\,e^{-iS(\mathbf{K},t)}, \quad (1)$$

$$\dot{n}_m(\mathbf{K},t) = is_m\,\Omega^*(\mathbf{K},t)\,\pi(\mathbf{K},t)\,e^{iS(\mathbf{K},t)} + \text{c.c.}, \quad (2)$$

where $\pi(\mathbf{K},t)$ denotes the interband polarization and $n_m(\mathbf{K},t)$ is the population in band m. The dephasing time T_2 characterizes the coherence decay of electron-hole pairs. The Rabi frequency is $\Omega(\mathbf{K},t) = \mathbf{E}(t)\cdot\mathbf{d}[\mathbf{K}+\mathbf{A}(t)]$, where $\mathbf{d}(\mathbf{k})$ is the interband transition-dipole vector and $\mathbf{E}(t)$ is the driving electric field. The population difference is $w(\mathbf{K},t) = n_C(\mathbf{K},t) - n_V(\mathbf{K},t)$, where C and V denote the conduction and valence bands, respectively. Here, $s_m = -1, +1$ for the VB and CB, respectively. The classical action is $S(\mathbf{K},t) = \int_{-\infty}^{t}\varepsilon_g[\mathbf{K}+\mathbf{A}(t')]\,dt'$, where ε_g is the interband transition energy. The crystal momentum $\mathbf{k}$ has been transformed into a frame comoving with the vector potential $\mathbf{A}(t) = -\int\mathbf{E}(t)\,dt$, so that $\mathbf{K} = \mathbf{k} - \mathbf{A}(t)$.

The total harmonic spectrum contains both intraband and interband contributions, with the total current $\mathbf{j}_{\text{tot}}(t) = \mathbf{j}_{\text{intra}}(t) + \mathbf{j}_{\text{inter}}(t)$. The intraband current, induced by carrier motion within individual bands, is

$$\mathbf{j}_{\text{intra}}(t) = \sum_{m=\text{c,v}}\int_{\text{BZ}}\mathbf{v}_m[\mathbf{K}+\mathbf{A}(t)]n_m(\mathbf{K},t)\,d^3\mathbf{K}, \quad (3)$$

where $\mathbf{v}_m(\mathbf{K}) = \nabla_{\mathbf{k}}E_m(\mathbf{K})$ is the carrier group velocity in band m, and the integral runs over the first BZ. The interband current is obtained from the time derivative of the interband polarization:

$$\mathbf{j}_{\text{inter}}(t) = \frac{d}{dt}\int_{\text{BZ}}\mathbf{d}[\mathbf{K}+\mathbf{A}(t)]\pi(\mathbf{K},t)e^{iS(\mathbf{K},t)}d^3\mathbf{K} + \text{c.c.} \quad (4)$$

In the one-dimensional (1D) two-band model along the Γ-M direction, the field-driven crystal momentum evolves as $\mathbf{k}(t) = \mathbf{K} + \mathbf{A}(t)$, and the emitted interband current is $j^{\parallel}_{\text{inter}}(t) = \hat{\mathbf{e}}\cdot\mathbf{j}_{\text{inter}}(t)$, where $\hat{\mathbf{e}}$ denotes the laser-polarization direction. Interband transitions dominate the harmonic emission in ZnO, consistent with previous studies [6,14,43–45]. The corresponding interband harmonic spectrum is therefore given by the Fourier transform of the interband current, $|\mathcal{F}[\mathbf{j}_{\text{inter}}(t)]|^2$.

Within the Keldysh approximation [$w(t)\approx 1$], the SBEs can be decoupled, and the interband transition can be expressed in the integral form

$$\mathbf{j}_{\text{inter}}(\omega_{\text{H}}) = \omega_{\text{H}}\int_{\text{BZ}}d^3\mathbf{k}\,\mathbf{d}(\mathbf{k})\int_{-\infty}^{\infty}dt\,e^{-i\omega_{\text{H}}t} \times\int_{-\infty}^{t}dt'\,\mathbf{E}(t')\cdot\mathbf{d}^*(\mathbf{k}_{t'})e^{-iS(\mathbf{k},t',t)-(t-t')/T_2} + \text{c.c.} \quad (5)$$

Here, ω_{H} denotes the emitted harmonic frequency, $\mathbf{k}_{t'} = \mathbf{k} + \mathbf{A}(t') - \mathbf{A}(t)$. The numerical implementation is benchmarked against the experimentally validated ZnO SBE calculations of Ref. [8].

B. Complex solutions of saddle-point equations

The saddle-point equations provide a quantitative framework for interpreting the microscopic mechanisms of solid-state HHG [14,15,39]. We analytically continue the real-valued interband integral in Eq. (5) into the complex domain using the stationary-phase approximation. The dominant contributions to the integral then arise from stationary points of the total phase. This analytical continuation establishes a direct link between the strong-field carrier dynamics encoded in the complex quantum trajectories and the macroscopic harmonic response obtained from the full SBE integration.

$$\frac{\partial}{\partial t_i}S(\mathbf{K},t_i,t_r) = \varepsilon_g[\mathbf{k}(t_i)] - \frac{i}{T_2} = 0, \quad (6)$$

$$\nabla_{\mathbf{K}}S(\mathbf{K},t_i,t_r) = \int_{t_i}^{t_r}d\tau\,\nabla_{\mathbf{K}}\varepsilon_g[\mathbf{k}(\tau)] = 0, \quad (7)$$

$$\frac{\partial}{\partial t_r}S(\mathbf{K},t_i,t_r) = \varepsilon_g[\mathbf{k}(t_r)] - \omega_{\text{H}} + \frac{i}{T_2} = 0, \quad (8)$$

where $S(\mathbf{K},t_i,t_r) = \int_{t_i}^{t_r}d\tau\,\varepsilon_g[\mathbf{k}(\tau)]$ is the semiclassical action, and t_i and t_r denote the ionization and recombination

times of the electron-hole trajectory. The crystal momentum evolves as $\mathbf{k}(t) = \mathbf{K} + \mathbf{A}(t)$, with $\mathbf{K}$ the canonical momentum and $\mathbf{A}(t) = -A_0 \sin(\omega t)$ the vector potential of the driving field. The interband transition energy is $\varepsilon_g[\mathbf{k}(t)] = \varepsilon_c[\mathbf{k}(t)] - \varepsilon_v[\mathbf{k}(t)]$. For the 1D two-band ZnO model along Γ-M, the band structure is expanded as $\varepsilon_g(k) = E_g + \sum_{j=0}^{5} \alpha_x^j \cos(jka_0)$, with lattice constant $a_0 = 5.32$ a.u. and coefficients α_x^j taken from Ref. [15].

The complex saddle-point solutions are written as $t_i = t_i' + it_i''$, $t_r = t_r' + it_r''$, and $\mathrm{K} = \mathrm{K}' + i\mathrm{K}''$ [38,40,46]. The ionization phase is $\phi_i = \omega t_i = \phi_i' + i\phi_i''$. Substituting t_i into Eq. (6) yields

$$E_g + \sum_{j=0}^{5} \alpha_x^j \cos(jx_1 + ijy_1) - \frac{i}{T_2} = 0, \tag{9}$$

where $x_1 = a_0(\mathrm{K}' - A_0 \sin\phi_i' \cosh\phi_i'')$ and $y_1 = a_0(\mathrm{K}'' - A_0 \cos\phi_i' \sinh\phi_i'')$.

We directly solve for (x_1, y_1) that satisfy Eq. (9). The canonical momentum components then read

$$\mathrm{K}'(\phi_i', \phi_i'') = A_0 \sin\phi_i' \cosh\phi_i'' + \frac{x_1}{a_0}, \tag{10}$$

$$\mathrm{K}''(\phi_i', \phi_i'') = A_0 \cos\phi_i' \sinh\phi_i'' + \frac{y_1}{a_0}. \tag{11}$$

Similarly, substituting the recombination phase $\phi_r = \omega t_r = \phi_r' + i\phi_r''$ into Eq. (8) gives

$$E_g - \omega_{\mathrm{H}} + \sum_{j=0}^{5} \alpha_x^j \cos(jx_2 + ijy_2) + \frac{i}{T_2} = 0, \tag{12}$$

with $x_2 = a_0(\mathrm{K}' - A_0 \sin\phi_r' \cosh\phi_r'')$ and $y_2 = a_0(\mathrm{K}'' - A_0 \cos\phi_r' \sinh\phi_r'')$. For $\omega_{\mathrm{H}} = n\omega \geqslant E_g$, where n is the harmonic order, we obtain

$$\mathrm{K}'(\phi_r', \phi_r'') = A_0 \sin\phi_r' \cosh\phi_r'' + \frac{x_2}{a_0}, \tag{13}$$

$$\mathrm{K}''(\phi_r', \phi_r'') = A_0 \cos\phi_r' \sinh\phi_r'' + \frac{y_2}{a_0}. \tag{14}$$

Combining Eqs. (10) and (11) with Eqs. (13) and (14), we derive

$$\phi_i'(\phi_r', \phi_r'') = \arcsin\sqrt{\frac{P - D}{2}}, \tag{15}$$

$$\phi_i''(\phi_r', \phi_r'') = \operatorname{arcosh}\sqrt{\frac{P + D}{2}}, \tag{16}$$

where

$$P = \left(\frac{\mathrm{K}' - \gamma'}{A_0}\right)^2 + \left(\frac{\mathrm{K}'' - \gamma''}{A_0}\right)^2 + 1,$$

$$D = \sqrt{P^2 - 4\left(\frac{\mathrm{K}' - \gamma'}{A_0}\right)^2}, \tag{17}$$

with $\gamma' = x_1/a_0$ and $\gamma'' = y_1/a_0$.

The physical origin of these complex quantities follows from the atomic HHG framework [40]. Equation (7) requires a condition satisfied trivially by classical trajectories but which carries nontrivial implications for quantum ones. The ionization condition $\varepsilon_g[k(t_i)] - i/T_2 = 0$ forces the electron kinetic energy at t_i to be close to the bandgap, so t_i is complex.

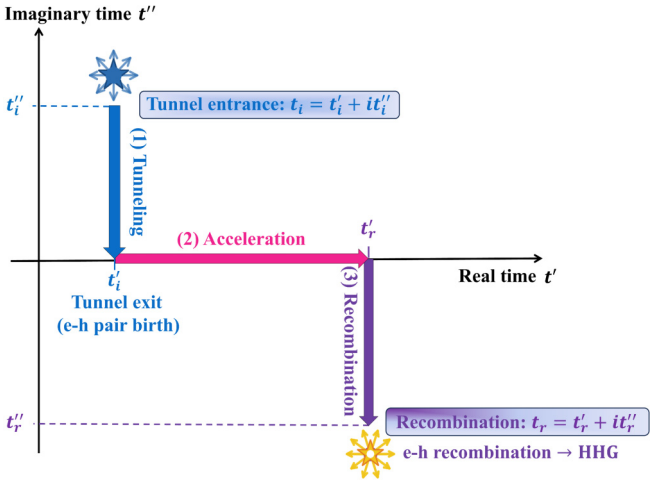

FIG. 1. Schematic illustration of the three-step model for solid-state HHG on the complex-time plane. (1) Tunneling: An electron tunnels from the VB to the CB. (2) Acceleration: The electron-hole pair is driven by the laser field. (3) Recombination: The pair recombines and emits a harmonic photon.

The displacement accumulated during underbarrier evolution from t_i to the real-time axis t_i' then yields a complex exit position: $\int_{t_i}^{t_i'} v(\mathrm{K}, \tau)\, d\tau = r_{\mathrm{ex}}' + ir_{\mathrm{ex}}''$ [40]. This imaginary exit displacement is a quantum signature of the tunneling process—It measures the spatial extent of wavefunction penetration through the classically forbidden bandgap region. To satisfy the zero-displacement recollision condition (7), the return time t_r and the canonical momentum K must acquire imaginary parts to compensate for r_{ex}''. In the solid-state context, K'' reflects the fact that the electron-hole pair has not been promoted to the conduction band as a free carrier; it retains an evanescent character linked to its tunneling birth. Unlike in photoelectron spectroscopy, where the detected electron momentum is real, in HHG the observable is the photon energy, so the electron canonical momentum may stay complex throughout the entire trajectory [40].

Figure 1 illustrates the resulting three-step picture on the complex-time plane. During tunneling, the electron is promoted from the VB to the CB, starting at the tunnel entrance $t_i = t_i' + it_i''$. The imaginary part of the ionization time encodes the tunneling duration, and the electron-hole pair emerges at the tunnel exit on the real-time axis t_i'. During acceleration, the pair is driven by the laser field along the real-time axis from t_i' to t_r'. Finally, recombination occurs at the complex saddle-point time $t_r = t_r' + it_r''$, where the emitted photon contributes a single harmonic to the HHG spectrum.

III. RESULTS AND DISCUSSION

In this paper, we consider a 1D two-band model along the Γ-M high-symmetry direction of ZnO. Additional calculations along the Γ-K direction yield the same qualitative trajectory assignment as those along Γ-M. Two-color fields provide a phase-sensitive interferometric probe of quantum trajectories in solids [32]. When a weak second-harmonic (SH) field is added to the fundamental field, inversion symmetry is broken, and even-order harmonics are activated. The

ω-2ω interferometric scheme requires the even-harmonic response to be nearly suppressed before the weak SH field is introduced. In the effective one-dimensional Γ-M geometry considered here, single-color excitation produces predominantly odd harmonics, so the weak SH field provides the dominant controlled symmetry breaking. Without this dynamical symmetry breaking, the even-order harmonics would remain suppressed, and no phase-delay maximum could be extracted. Along an intrinsically asymmetric direction such as Γ-A, medium-induced even harmonics would coexist with the SH-induced contribution, and the simple relation $I_{2N} \propto |\sin\sigma|^2$ would no longer apply. The phase accumulated by an electron-hole trajectory due to the weak SH perturbation is written as

$$\sigma(\mathbf{K}, t_i, t_r, \phi) = -\int_{t_i}^{t_r} \mathbf{v}(\tau, \mathbf{K}) \cdot \mathbf{A}_{2\omega}(\tau, \phi)\, d\tau. \tag{18}$$

Here, $\mathbf{A}_{2\omega}$ is the vector potential of the SH field, and $\mathbf{v}(\mathbf{k}) = \nabla_{\mathbf{k}}\varepsilon_g(\mathbf{k})$ denotes the relative velocity of the electron with respect to the hole. Here, ϕ denotes the relative phase of the 2ω field. Within the quantum-trajectory model, the odd- and even-order yields follow $|\cos\sigma|^2$ and $|\sin\sigma|^2$, respectively [8,34,38]. As a result, the even-order harmonics are much more sensitive to the relative two-color phase, whereas the odd-order response varies only weakly near the modulation extrema:

$$I(n\omega) \propto \begin{cases} |\cos[\sigma(\mathbf{K}, t_i, t_r, \phi)]|^2, & n \text{ is odd}, \\ |\sin[\sigma(\mathbf{K}, t_i, t_r, \phi)]|^2, & n \text{ is even}. \end{cases} \tag{19}$$

Equation (19) determines the relative phase $\phi_{\max}$ at which the even-order harmonic yield is maximal. This framework establishes a quantitative link between the measured harmonic modulation and the underlying ionization-recombination trajectory. Previous studies showed that quantum-trajectory calculations reproduce two-color interferometry and SBE results well for higher-order harmonics [38,39], but noticeable discrepancies remain in the low-order region. Here, we focus on these near-bandgap harmonics. To enable direct comparison, we adopt the same laser parameters as in the experiment and in earlier theoretical work [8,39]. We use a linearly polarized driving field $E(t) = E_0\cos(\omega t)$ with an amplitude of $E_0 = \omega A_0 = 0.008$ a.u., consistent with $\mathbf{A}(t) = -A_0\sin(\omega t)$. The ω-2ω interferometric scheme requires a multicycle fundamental field with approximate half-cycle symmetry, $E_\omega(t + T/2) \simeq -E_\omega(t)$. We therefore employ a 16-cycle flat-top pulse to enable a clean extraction of the trajectory-dependent phase-delay maximum $\phi_{\max}$. Additional truncated-Gaussian calculations confirm that the trajectory assignment and $\phi_{\max}$ remain robust within the multicycle regime. The laser wavelength is $\lambda = 3250$ nm ($\hbar\omega \simeq 0.38$ eV), while the minimum direct bandgap of ZnO is $E_g \simeq 3.37$ eV, corresponding approximately to the ninth harmonic. We therefore focus on the 10th–12th harmonic region, particularly the even 10th and 12th harmonics, which provide the most sensitive above-gap observables for the present interband trajectory analysis. In the selected 10th–12th harmonic region, the interband contribution dominates the total harmonic response. The intraband current may modify the absolute yield and modulation contrast, but the phase-delay maxima are therefore expected to remain governed by the interband dynamics and to retain the same trajectory assignment. Using the saddle-point solutions, we determine the ionization time t_i, recombination time t_r, and canonical momentum $\mathbf{K}$ for each trajectory branch. The relative phase $\phi_{\max}$ corresponding to the maximum even-harmonic intensity is then calculated from $I_{2N}^{\max} \propto |\sin[\sigma(\mathbf{K}, t_i, t_r, \phi_{\max})]|^2$. In Fig. 2(a), the bright ridges indicate the SBE modulation maxima, while the discrete magenta and cyan markers denote the corresponding normalized delay positions predicted by the conventional short and delayed multiple-scattering trajectories, respectively. The short-trajectory markers agree with the SBE maxima at higher orders but deviate in the near-bandgap region, whereas the multiple-scattering markers agree with the near-bandgap harmonics but not with the higher orders. Figure 2(b) shows the time-frequency distribution of the harmonic emission at the center of the monochromatic-field plateau. For higher orders ($n \gtrsim 14$), the emission concentrates along the short trajectory. The near-bandgap harmonics, in contrast, have a broader emission window and are not captured by the short-trajectory picture, pointing to a delayed dynamical channel beyond the simplest return process. Pump-power scaling supports the nonperturbative character of both near-bandgap and higher-order harmonics but cannot distinguish their microscopic trajectories. Unlike power scaling, the ω-2ω interferometer is sensitive to the ionization and recombination times through the trajectory-dependent phase $\sigma = -\int_{t_i}^{t_r} \mathbf{v}(\tau, \mathbf{K}) \cdot \mathbf{A}_{2\omega}(\tau, \phi)\, d\tau$, enabling the conventional

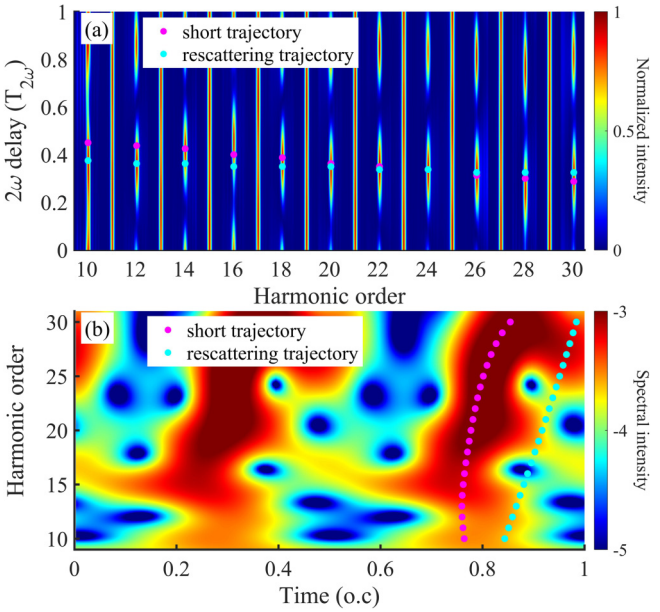

FIG. 2. (a) Harmonic yield as a function of harmonic order and relative phase delay between the fundamental and SH fields, where the delay is given in units of the SH optical period $T_{2\omega}$. The color scale shows the normalized harmonic intensity. (b) Time-frequency analysis of harmonic emission from ZnO. The color scale shows the logarithm of the harmonic intensity in arbitrary units. Time is given in optical cycles. The discrete magenta and cyan markers denote the relative phases $\phi_{\max}$ corresponding to the maximum even-harmonic intensities predicted by the conventional short and delayed multiple-scattering trajectories, respectively. These markers are compared directly with the bright modulation maxima in the SBE map.

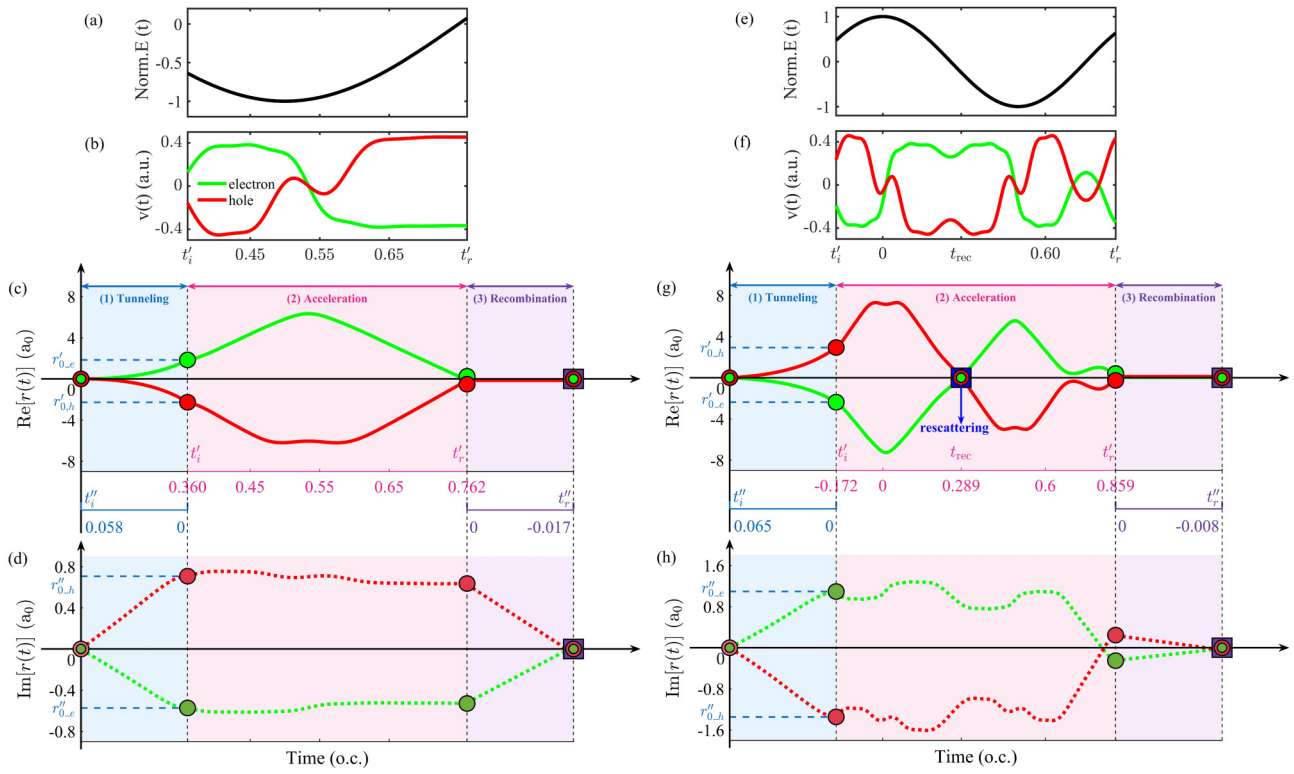

FIG. 3. Time-dependent quantum trajectories of the electron-hole pair for a short trajectory [left column, panels (a)–(d)] and a rescattering trajectory [right column, panels (e)–(h)]. (a), (e) Normalized electric field $E(t)$. (b), (f) Real-time velocities of the electron (green) and hole (red) during the acceleration step. (c), (g) Real part of the electron and hole displacements, $\mathrm{Re}[r(t)]$. The shaded regions indicate the three dynamical stages: tunneling (blue, $t_i'' \to 0$), acceleration (pink, $t_i' \to t_r'$), and recombination (lavender, $0 \to t_r''$). (d), (h) Same as panels (c) and (g), but for the imaginary part of the displacements, $\mathrm{Im}[r(t)]$.

short and delayed multiple-scattering trajectories to be distinguished by their phase-delay maxima. Independently, the time-frequency analysis shows that the near-bandgap harmonics have a broader and delayed emission window, whereas the higher-order harmonics follow the short-trajectory branch. Such a timing difference is not accessible from pump-power scaling alone, but is resolved by the time-frequency and ω-2ω phase-delay analyses.

To clarify the physical origin of the near-bandgap harmonics, we further analyze electron-hole trajectories that are launched in the preceding optical cycle. These delayed trajectories undergo extended laser-driven motion before recombination and are repeatedly redirected by the periodic band structure and the laser field. As shown in Fig. 2(a), such an earlier-born trajectory provides the missing contribution to the near-bandgap harmonic emission. This comparison motivates the detailed analysis of the earlier-born multiple-scattering trajectory below. In the time-frequency domain [Fig. 2(b)], the multiple-scattering trajectory captures the overall delayed emission structure of the near-bandgap harmonics, although residual deviations from the full SBE result remain. These deviations are expected because the present two-trajectory description does not include interference among all contributing quantum paths, all of which can broaden and reshape the low-order emission window. In this sense, near-bandgap harmonics in solids are analogous to near-threshold harmonics in atoms—both require a return picture beyond the short trajectory [18–25]. The underlying mechanism, however, is fundamentally different. In atoms, rescattering is governed by the long-range Coulomb potential of the parent ion. In the crystal studied here, the delayed return is instead induced by the periodic band structure and consists of repeated Bragg scattering at the BZ boundary together with electron-hole reencounter near the Γ point, where their relative motion is reversed before final recombination.

Figure 3 compares the time-dependent dynamics of the short and rescattering trajectories. In both cases, the electron-hole pair acquires a nonzero initial velocity [see Figs. 3(b) and 3(f)], a finite initial real-space separation [see Figs. 3(c) and 3(g)], and a substantial imaginary displacement [see Figs. 3(d) and 3(h)] during the tunneling process. Upon completion of the tunneling process, the initial electron and hole displacements can be determined as $r_{0,[e,h]} = \int_{t_i}^{t_i'} v_{[e,h]}(\mathrm{K}, \tau)\, d\tau = r'_{[e,h]} + i r''_{[e,h]}$. The electron (green) and hole (red) are born at t_i' with initial real displacements $r'_{0,e}$ and $r'_{0,h}$ [dashed blue lines in Figs. 3(c) and 3(g)] and initial imaginary displacements $r''_{0,e}$ and $r''_{0,h}$ [dashed blue lines in Figs. 3(d) and 3(h)]. The real part describes the laser-driven electron-hole separation in real space, whereas the imaginary part carries the residual memory of the tunneling process.

For the short trajectory [Figs. 3(a)–3(d)], tunneling and recombination occur within the same optical cycle. During the acceleration stage from t_i' to t_r', the imaginary displacement remains nearly constant, while the real-space separation first increases and then decreases. At the real time t_r', i.e., $\mathrm{Re}(t_r)$, however, the electron and hole do not exactly overlap in real

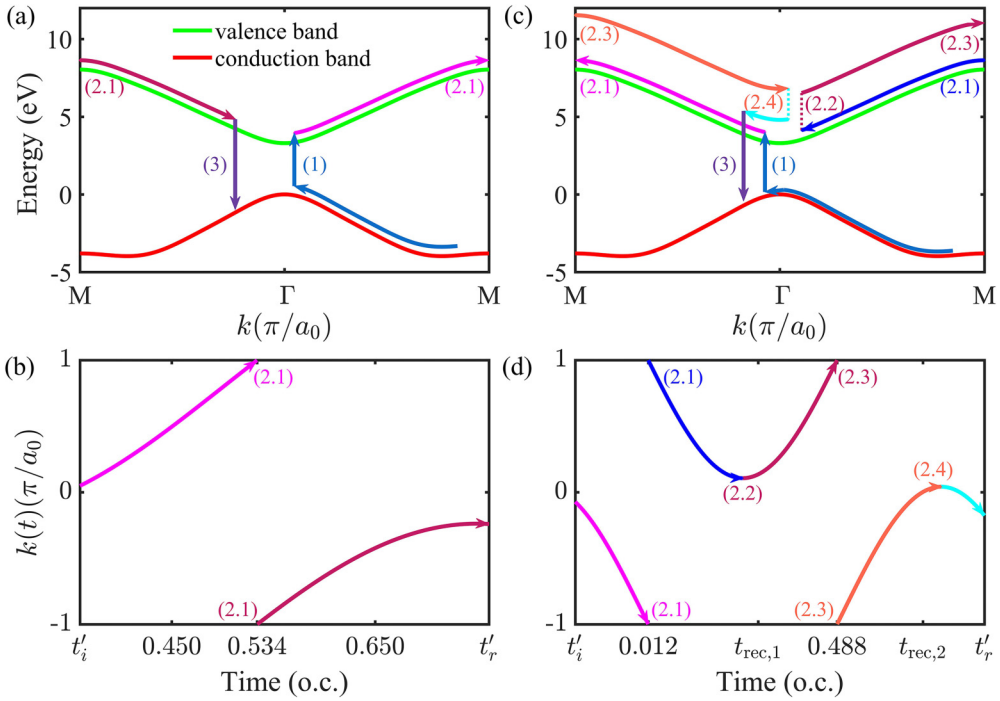

FIG. 4. Band-resolved k-space trajectories (upper row) and time-dependent crystal momentum $k(t)$ (lower row) along the M-Γ-M direction for a short trajectory [left column, panels (a) and (b)] and a rescattering trajectory [right column, panels (c) and (d)]. The band-resolved trajectories in panels (a) and (c) show the electron-hole dynamics on the CB (green) and VB (red) structures. The three dynamical processes are labeled as (1) tunneling, (2) acceleration, and (3) recombination. In the short trajectory [panels (a) and (b)], (2.1) marks the single Bragg scattering at the BZ boundary. In the rescattering trajectory [panels (c) and (d)], (2.1) and (2.3) indicate successive Bragg scatterings, whereas (2.2) and (2.4) mark electron-hole reencounter events near the Γ point.

space. This is consistent with earlier treatments of "imperfect recollisions" [47,48]. However, in those treatments, the electron-hole separation at recollision is usually inferred from a real-time semiclassical estimate, whereas here we explicitly obtain the real-time electron and hole positions from the complex saddle-point construction. As seen in Fig. 3(c), the electron and hole displacements at t_r' are -0.65 and -0.77 a.u., respectively, corresponding to a finite real-space separation of about 0.12 a.u. between the electron and the hole at the real recombination time, which is not the final recombination point. It is further compensated during the subsequent quantum recombination step, which is the inverse process of tunneling ionization and takes place along the imaginary-time axis. This stage has no classical real-time counterpart and should therefore be regarded as a purely quantum part of the HHG trajectory, as sketched in Fig. 1. Thus, the HHG trajectory contains two quantum steps associated with real-space displacement: Tunneling creates a finite electron-hole separation, while recombination removes the electron-hole separation and brings the real-space electron-hole displacement exactly back to zero after photon emission.

The multiple-scattering trajectory [Figs. 3(e)–3(h)] behaves differently. Because the electron-hole pair is born one optical cycle earlier, it accumulates larger real and imaginary displacements before final recombination. More importantly, Fig. 3(g) shows that the real part of the relative displacement first reaches zero at $t_{\mathrm{rec},1} \approx 0.289$ o.c., indicating that the electron and hole overlap in real space at this instant. However, Fig. 3(h) shows that a large imaginary displacement still remains. This means that the electron and hole have not truly recombined in the full complex trajectory. Instead, they merely pass by each other in real space, which is analogous to the rescattering of an electron with the core in atomic gases [18–25]. Another real-space reencounter of the electron-hole pair occurs again at $t_{\mathrm{rec},2} \approx 0.704$ o.c., also with a nonzero imaginary displacement, indicating that it is still a rescattering process rather than recombination.

This perspective yields a physically transparent criterion for coherent recombination. True stationary-phase recombination occurs only during the final complex-time recombination step, where the real and imaginary parts of the relative displacement vanish simultaneously. If the imaginary component is still finite when the real displacement vanishes, as seen in the rescattering trajectory at $t_{\mathrm{rec},[1,2]}$, the pair has merely undergone scattering-induced spatial overlap and does not satisfy the full complex saddle condition.

The reciprocal-space trajectories in Fig. 4 clarify the origin of these electron-hole rescattering events. For the short trajectory [Figs. 4(a) and 4(b)], the crystal momentum reaches the BZ boundary only once, as labeled by process (2.1). This event is a Bragg scattering in which the periodic crystal potential folds the crystal momentum back into the first BZ and reverses the relative electron-hole motion, thereby driving the pair back toward recombination.

For the multiple-scattering trajectory [Figs. 4(c) and 4(d)], the electron-hole pair undergoes a sequence of momentum-space redirections before final recombination. The processes

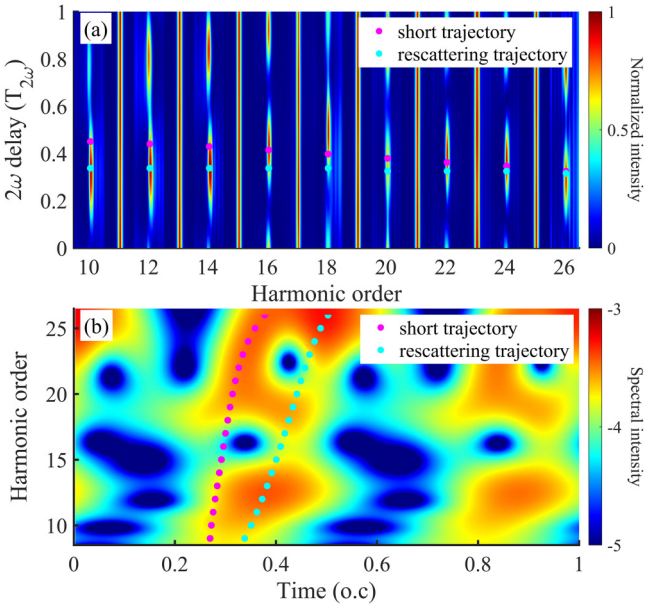

FIG. 5. Same as Fig. 2, except that the driving wavelength is set to $\lambda = 2800$ nm. The overlaid magenta and cyan markers denote the conventional short and delayed multiple-scattering trajectories, respectively.

labeled as (2.1) and (2.3) occur at the BZ boundary and correspond to Bragg scattering. These boundary events fold the crystal momentum back into the first BZ and redirect the relative electron-hole motion [49]. The electron-hole rescattering mainly occurs in the subsequent Γ point-turning stage, i.e., during the processes (2.2) and (2.4). This stage corresponds to the real-space electron-hole reencounter. However, as shown in Fig. 3(h), a large imaginary displacement still remains. The electron and hole therefore only pass by each other in real space rather than recombine. True stationary-phase recombination occurs only later, when both the real and imaginary parts of the relative displacement vanish simultaneously.

To test the robustness of this interpretation, we further consider a shorter driving wavelength of 2800 nm, as shown in Fig. 5. Again, the rescattering trajectory reproduces 10th- and 12th-order harmonics, while the short trajectory continues to describe the higher-order harmonics. The time-frequency analysis in Fig. 5(b) shows that the near-bandgap harmonics retain a delayed and broader emission window, with the delayed multiple-scattering component appearing approximately 0.05–0.10 optical cycles later than the short-trajectory emission. These results are consistent with the same trajectory assignment at the shorter driving wavelength. A quantitative decomposition of the relative intensities of different trajectories, however, requires reliable complex saddle-point prefactors that incorporate transition dipoles, dephasing, and interference between quantum paths. Developing such an amplitude-resolved trajectory framework remains an important direction for future work.

IV. CONCLUSION

We have investigated the microscopic origin of near-bandgap harmonic generation in ZnO using a complex-time quantum-trajectory framework combined with semiconductor Bloch equations. By retaining both tunneling and multiple scattering, we find a clear dynamical distinction between higher-order and near-bandgap harmonics.

Near-bandgap harmonics are associated with delayed multiple-scattering trajectories involving Bragg scattering at the BZ boundary and electron-hole reencounters near the Γ point. A vanishing real-space separation is not, by itself, sufficient for coherent recombination. Within the two-band framework, stationary-phase recombination requires the imaginary component of the relative displacement to simultaneously decay to zero. This criterion extends to solid-state HHG the complex-trajectory insight of Smirnova and Ivanov [40]: The imaginary displacement is a persistent quantum fingerprint of tunneling, and its compensation is a prerequisite for coherent emission.

These results provide a clear physical picture of near-bandgap HHG in solids and highlight the value of complex quantum trajectories for analyzing phase-resolved strong-field dynamics. The imaginary part of the electron-hole displacement may also serve as a diagnostic for identifying recombination pathways in other semiconductor systems.

ACKNOWLEDGMENTS

This work was supported by the National Natural Science Foundation of China (Grants No. 12534010, No. 12374260, No. 12574310, No. 12574285, and No. 12447177), the Hainan Provincial Science and Technology Talent Innovation Project (Grant No. KJRC2025B13), Hainan Provincial Natural Science Foundation (Grant No. 125RC626), and Collaborative Innovation Center of Tropical Marine Science and Technology, Hainan University (Grant No. XTCX2022HYC27).

DATA AVAILABILITY

There are no publicly available research data or software supporting this manuscript. Requests for further information or data should be sent to the authors.

[1] F. Krausz and M. Ivanov, Attosecond physics, Rev. Mod. Phys. **81**, 163 (2009).

[2] R. Weissenbilder, S. Carlström, L. Rego, C. Guo, C. M. Heyl, P. Smorenburg, E. Constant, C. L. Arnold, and A. L' Huillier, How to optimize high-order harmonic generation in gases, Nat. Rev. Phys. **4**, 713 (2022).

[3] M. Hentschel, R. Kienberger, C. Spielmann, G. A. Reider, N. Milosevic, T. Brabec, P. Corkum, U. Heinzmann, M. Drescher,

and F. Krausz, Attosecond metrology, Nature (London) **414**, 509 (2001).

[4] P.-M. Paul, E. S. Toma, P. Breger, G. Mullot, F. Augé, P. Balcou, H. G. Muller, and P. Agostini, Observation of a train of attosecond pulses from high harmonic generation, Science **292**, 1689 (2001).

[5] P. B. Corkum, Plasma perspective on strong-field multiphoton ionization, Phys. Rev. Lett. **71**, 1994 (1993).

[6] S. Ghimire, A. D. DiChiara, E. Sistrunk, P. Agostini, L. F. DiMauro, and D. A. Reis, Observation of high-order harmonic generation in a bulk crystal, Nat. Phys. **7**, 138 (2011).

[7] S. Ghimire and D. A. Reis, High-harmonic generation from solids, Nat. Phys. **15**, 10 (2019).

[8] G. Vampa, T. J. Hammond, N. Thiré, B. E. Schmidt, F. Légaré, C. R. McDonald, T. Brabec, and P. B. Corkum, Linking high harmonics from gases and solids, Nature (London) **522**, 462 (2015).

[9] F. Langer, M. Hohenleutner, U. Huttner, S. W. Koch, M. Kira, and R. Huber, Symmetry-controlled temporal structure of high-harmonic carrier fields from a bulk crystal, Nat. Photon. **11**, 227 (2017).

[10] S. M. Cavaletto, K. M. Kowalczyk, F. O. Navarrete, and J. Rivera-Dean, The attoscience of strong-field-driven solids, Nat. Rev. Phys. **7**, 38 (2025).

[11] C. Heide, Y. Kobayashi, S. R. U. Haque, and S. Ghimire, Ultrafast high-harmonic spectroscopy of solids, Nat. Phys. **20**, 1546 (2024).

[12] A. Jiménez-Galán, C. Bossaer, G. Ernotte, A. M. Parks, R. E. F. Silva, D. M. Villeneuve, A. Staudte, T. Brabec, A. Luican-Mayer, and G. Vampa, Orbital perspective on high-harmonic generation from solids, Nat. Commun. **14**, 8421 (2023).

[13] T. T. Luu, M. Garg, S. Y. Kruchinin, A. Moulet, M. Th. Hassan, and E. Goulielmakis, Extreme ultraviolet high-harmonic spectroscopy of solids, Nature (London) **521**, 498 (2015).

[14] G. Vampa, C. R. McDonald, G. Orlando, D. D. Klug, P. B. Corkum, and T. Brabec, Theoretical analysis of high-harmonic generation in solids, Phys. Rev. Lett. **113**, 073901 (2014).

[15] G. Vampa, C. R. McDonald, G. Orlando, P. B. Corkum, and T. Brabec, Semiclassical analysis of high harmonic generation in bulk crystals, Phys. Rev. B **91**, 064302 (2015).

[16] T. Y. Du and X. B. Bian, Quasi-classical analysis of the dynamics of the high-order harmonic generation from solids, Opt. Express **25**, 151 (2017).

[17] Y. W. Kim, T. J. Shao, H. Kim, S. Han, S. Kim, M. Ciappina, X. B. Bian, and S. W. Kim, Spectral interference in high harmonic generation from solids, ACS Photon. **6**, 851 (2019).

[18] W. H. Xiong, J. W. Geng, J. Y. Tang, L. Y. Peng, and Q. Gong, Mechanisms of below-threshold harmonic generation in atoms, Phys. Rev. Lett. **112**, 233001 (2014).

[19] J. A. Hostetter, J. L. Tate, K. J. Schafer, and M. B. Gaarde, Semiclassical approaches to below-threshold harmonics, Phys. Rev. A **82**, 023401 (2010).

[20] J. Heslar and S. I. Chu, Probing multirescattering dynamics and electron quantum paths for below- and near-threshold harmonic generation of H_2 in an intense laser field, Phys. Rev. A **95**, 043414 (2017).

[21] P. C. Li, Y. L. Sheu, C. Laughlin, and S. I. Chu, Dynamical origin of near- and below-threshold harmonic generation of Cs in an intense mid-infrared laser field, Nat. Commun. **6**, 7178 (2015).

[22] P. C. Li, Y. L. Sheu, C. Laughlin, and S. I. Chu, Role of laser-driven electron-multirescattering in resonance-enhanced below-threshold harmonic generation in He atoms, Phys. Rev. A **90**, 041401(R) (2014).

[23] B. Wang, Y. Zhang, P. Lan, C. Zhai, M. Li, X. Zhu, J. Chen, P. Lu, and C. D. Lin, Anomalous ellipticity dependence of the generation of near-threshold harmonics in noble gases, Phys. Rev. A **103**, 053119 (2021).

[24] P. C. Li, Z. B. Wang, and S. I. Chu, Multichannel-resolved dynamics in resonance-enhanced below-threshold harmonic generation of H_2^+ molecular ions, Phys. Rev. A **103**, 043113 (2021).

[25] P. C. Li, Y. L. Sheu, H. Z. Jooya, X. X. Zhou, and S. I. Chu, Exploration of laser-driven electron-multirescattering dynamics in high-order harmonic generation, Sci. Rep. **6**, 32763 (2016).

[26] E. A. Bleda, I. Yavuz, Z. Altun, and T. Topcu, High-order harmonic generation from Rydberg states at fixed Keldysh parameter, Phys. Rev. A **88**, 043417 (2013).

[27] H. Soifer, P. Botheron, D. Shafir, A. Diner, O. Raz, B. D. Bruner, Y. Mairesse, B. Pons, and N. Dudovich, Near-threshold high-order harmonic spectroscopy with aligned molecules, Phys. Rev. Lett. **105**, 143904 (2010).

[28] N. Mayer, S. Beaulieu, Á. Jiménez-Galán, S. Patchkovskii, O. Kornilov, D. Descamps, S. Petit, O. Smirnova, Y. Mairesse, and M. Y. Ivanov, Role of spin-orbit coupling in high-order harmonic generation revealed by supercycle Rydberg trajectories, Phys. Rev. Lett. **129**, 173202 (2022).

[29] G. Vampa and T. Brabec, Merge of high harmonic generation from gases and solids and its implications for attosecond science, J. Phys. B: At. Mol. Opt. Phys. **50**, 083001 (2017).

[30] P. Jürgens, B. Liewehr, B. Kruse, C. Peltz, D. Engel, A. Husakou, T. Witting, M. Ivanov, M. J. J. Vrakking, T. Fennel, and A. Mermillod-Blondin, Origin of strong-field-induced low-order harmonie generation in amorphous quartz, Nat. Phys. **16**, 1035 (2020).

[31] A. Nayak, M. Dumergue, S. Kühn, S. Mondal, T. Csizmadia, N. G. Harshitha, M. Füle, M. U. Kahaly, B. Farkas, B. Major, *et al.*, Saddle point approaches in strong field physics and generation of attosecond pulses, Phys. Rep. **833**, 1 (2019).

[32] T. T. Luu and H. J. Wörner, Observing broken inversion symmetry in solids using two-color high-order harmonic spectroscopy, Phys. Rev. A **98**, 041802(R) (2018).

[33] O. Kneller, D. Azoury, Y. Federman, M. Krüger, A. J. Uzan, G. Orenstein, B. D. Bruner, O. Smirnova, S. Patchkovskii, M. Ivanov, and N. Dudovich, A look under the tunnelling barrier via attosecond-gated interferometry, Nat. Photon. **16**, 304 (2022).

[34] A. J. Uzan-Narovlansky, A. Jiménez-Galán, G. Orenstein, R. E. F. Silva, T. Arusi-Parpar, S. Shames, B. D. Bruner, B. Yan, O. Smirnova, M. Ivanov, and N. Dudovich, Observation of light-driven band structure via multiband high-harmonic spectroscopy, Nat. Photon. **16**, 428 (2022).

[35] M. Krüger and N. Dudovich, Attosecond interferometry, in *Ultrafast Electronic and Structural Dynamics*, edited by K. Ueda (Springer, Singapore, 2024), pp. 45–71.

[36] T. Helk, E. Berger, S. Jamnuch, L. Hoffmann, A. Kabacinski, J. Gautier, F. Tissandier, J.-P. Goddet, H.-T. Chang, J. Oh, C. D. Pemmaraju, T. A. Pascal, S. Sebban, C. Spielmann, and M. Zuerch, Table-top extreme ultraviolet second harmonic generation, Sci. Adv. **7**, eabe2265 (2021).

[37] O. Pedatzur, G. Orenstein, V. Serbinenko, H. Soifer, B. D. Bruner, A. J. Uzan, D. S. Brambila, A. G. Harvey, L. Torlina, F. Morales, O. Smirnova, and N. Dudovich, Attosecond tunnelling interferometry, Nat. Phys. **11**, 815 (2015).

[38] G. Vampa, J. Lu, Y. S. You, D. R. Baykusheva, M. Wu, H. Liu, K. J. Schafer, M. B. Gaarde, D. A. Reis, and S. Ghimire, Attosecond synchronization of extreme ultraviolet high harmonics from crystals, J. Phys. B: At. Mol. Opt. Phys. **53**, 144003 (2020).

[39] R. Zuo, X. Song, S. Ben, T. Meier, and W. Yang, Revealing the nonadiabatic tunneling dynamics in solid-state high harmonic generation, Phys. Rev. Res. **5**, L022040 (2023).

[40] O. Smirnova and M. Ivanov, Multielectron high harmonic generation: Simple man on a complex plane, in *Attosecond, XUV Physics: Ultrafast Dynamics, Spectroscopy*, edited by T. Schultz and M. Vrakking (Wiley-VCH, Weinheim, 2014), Chap. 7, pp. 201–256.

[41] D. Golde, T. Meier, and S. W. Koch, High harmonics generated in semiconductor nanostructures by the coupled dynamics of optical inter- and intraband excitations, Phys. Rev. B **77**, 075330 (2008).

[42] H. Haug and S. W. Koch, *Quantum Theory of the Optical and Electronic Properties of Semiconductors*, 5th ed. (World Scientific, Singapore, 2009).

[43] Z. Guan, X. X. Zhou, and X. B. Bian, High-order-harmonic generation from periodic potentials driven by few-cycle laser pulses, Phys. Rev. A **93**, 033852 (2016).

[44] G. Wang, Y.-X. Chen, M. Li, and T.-Y. Du, High-order harmonic spectroscopy for probing intraband and interband dynamics, Phys. Rev. A **109**, 063511 (2024).

[45] Z. Wang, H. Park, Y. H. Lai, J. Xu, C. I. Blaga, F. Yang, P. Agostini, and L. F. DiMauro, The roles of photo-carrier doping and driving wavelength in high harmonic generation from a semiconductor, Nat. Commun. **8**, 1686 (2017).

[46] J. Liu, S. Jiang, J. Chen, L. He, J. Wang, and X. Zhao, Complex saddle point analysis of solid high order harmonic generation and reconstruction of dephasing time, APL Comput. Phys. **1**, 026104 (2025).

[47] L. Yue and M. B. Gaarde, Imperfect recollisions in high-harmonic generation in solids, Phys. Rev. Lett. **124**, 153204 (2020).

[48] L. Yue and M. B. Gaarde, Expanded view of electron-hole recollisions in solid-state high-order harmonic generation: Full-Brillouin-zone tunneling and imperfect recollisions, Phys. Rev. A **103**, 063105 (2021).

[49] C. M. Wang, N. Tancogne-Dejean, M. Altarelli, A. Rubio, and S. A. Sato, Role of electron scattering on the high-order harmonic generation from solids, Phys. Rev. Res. **2**, 033333 (2020).